CL00-0388

Wavefront Control for a Segmented Deployable Space Telescope

David Redding,* Scott Basinger,* David Cohen,* Andrew Lowman,* Fang Shi,* Pierre Bely,† Chuck Bowers,‡ Richard Burg,‡ Laura Burns,‡ Pamela Davila,‡ Bruce Dean,‡ Gary Mosier,‡ Todd Norton,‡ Pete Petrone,‡ Brendon Perkins,‡ Mark Wilson‡

ABSTRACT

By segmenting and folding the primary mirror, quite large telescopes can be packed into the nose cone of a rocket. Deployed after launch, initial optical performance can be quite poor, due to deployment errors, thermal deformation, fabrication errors and other causes. We describe an automatic control system for capturing, aligning, phasing, and deforming the optics of such a telescope, going from initial cm-level wavefront errors to diffraction-limited observatory operations. This system was developed for the Next Generation Space Telescope and is being tested on the NGST Wavefront Control Testbed.

1.INTRODUCTION

The Next Generation Space Telescope (NGST), to be launched in 2008, will provide an 8 m aperture space telescope for imagery and spectrometry from about 1 um to 16 um wavelength. 1-2 (Fig. 1). The primary mirror will be segmented in order to fit it into a launch vehicle, then deployed after launch. At first light, following deployment, optical aberrations are expected to be large. Alignment shifts during launch, deployment errors, thermal deformations, mirror fabrication errors, and other effects can combine to cause initial wavefront errors of several millimeters. The wavefront control (WFC) system described here is used to capture, align, phase and deform the primary mirror segments and other optics to remove these initial errors and establish diffraction limited performance for science observations. After observatory commissioning, the WFC fine-phasing mode will be used periodically, as needed to keep the optical performance within specifications. Because NGST will be in a highly stable environment, with careful dynamical and thermal isolation and control this interval is expected to be quite long, days to months.

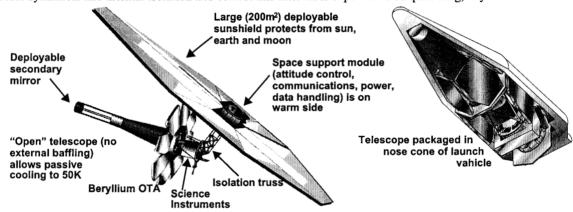


Figure 1. NGST Yardstick configuration.

This paper summarizes and updates the baseline NGST WFC subsystem. Previous papers have reported WFC performance in a range of NGST simulations³ and from experiments conducted on the NGST WFC Testbed (WCT, aka DCATT).⁴ The emphasis here is on reporting new results, illustrating performance with data from the testbed and from simulations. More detail of the WFC system and its performance is presented in 3 companion papers.^{5,6,7} The WCT is described in more detail in other papers.^{8,9}

The baseline NGST WFC has 4 distinct modes: Capture and Alignment; Reference Segment Alignment; Coarse Phasing; and Fine Phasing, as sketched in Fig. 2.

The first mode, Capture and Alignment, begins with the segments deployed to mechanical tolerances and the telescope pointed at a bright, isolated calibration star using startrackers. The large initial errors have the effect of breaking up the image of the star into multiple pale fuzzy blobs – defocussed segment images – which may not even fall onto the detector. The Capture and Alignment controller scans each segment in tilt until its blob is moved into the field of view and so is identified. The segment image is then focussed (to within the segment depth of focus), and coarsely aligned.

^{*} Jet Propulsion Laboratory, California Institute of Technology, Pasadena CA 91109

[†] Space Telescope Science Institute, Baltimore MD

[†] Goddard Space Flight Center, National Aeronautics and Space Administration, Greenbelt MD

Reference Segment Alignment aligns the "reference segment" – the center segment in most configurations – to the secondary mirror, tertiary mirror, and instrument module. This can be done using traditional focus/coma sweep techniques, with the other segments tilted away from the center of the FOV; using prescription retrieval techniques; ¹⁰ or using wavefront sensing as in the Fine Phasing control mode. When aligned, the reference segment is taken as fixed, and the other segments are aligned and phased to it in sequence.

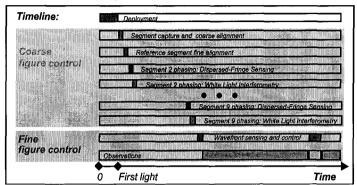


Figure 2. Wavefront control timeline.

Coarse Phasing control combines 2 sensing techniques. Dispersed-Fringe Sensing accurately measures large segment-to-segment pathlength differences by using a grism to disperse the light from dephased segments, modulating a fixed pathlength difference by a varying wavelength. It provides an accurate, robust phasing signal over about 1 mm of piston error. White-Light Interferometry, which generates fringes by scanning one segment in piston, is a more sensitive measure when the pathlength differences are small. At the end of Coarse Phasing, the initial millimetric error has been reduced to the sub-micron level.

The final active control step, *Fine Phasing* control, utilizes iterative-transform focus-diverse phase retrieval wavefront sensing to produce a high-resolution estimate of the wavefront. The estimate is used for wavefront control, driving deformable mirrors and segment alignments to achieve diffraction-limited performance. Fine Phasing is repeated periodically during the mission.

Figure and alignment will be held passively during observations. This is possible because of the high degree of stability designed into the NGST mission. The benign L2 environment, extensive thermal shielding, and careful structural and thermal design (possibly including thermal control) keep NGST from experiencing large deformations and load changes on-orbit. Vibration isolation and careful maneuver planning keep dynamical disturbances at a low level. These and other measures permit long times between Fine Phasing updates, days to months.

Telescope guiding prior to Fine Phasing is by startracker-referenced spacecraft attitude control, with an accuracy of about 1 asec. FSM fine guiding begins before Fine Phasing. The FSM stabilizes a guide star in one of the 4 NIR camera channels, while WF sensing is conducted in another channel. The detector is windowed to permit 100 frames/sec readout rates. The FSM closed-loop bandwidth is about 10 Hz. The ACS follows-up the FSM control at below 0.01 Hz bandwidth, keeping the FSM stroke small. Predicted jitter is under about 1/5th of a pixel, a few milliarcsec. 11

2.SYSTEM DESCRIPTION

There are several different NGST configurations being pursued by the various NGST architecture teams. The NASA "government team" has concentrated on a point design, called the NGST "Yardstick" configuration, for studies of feasibility, performance and technology readiness. The Yardstick, illustrated in Fig. 1, uses 9 segments in a "flower" pattern to form its primary mirror. The outer segments are folded – some up, some down – to fit into the launch vehicle shroud. Once on orbit, they deploy, each in a single rotation. All segments are actuated in at least 3 rigid-body DOFs; they may be equipped with deforming actuators as well. The SM is mounted on a deployed 4-strut tower, attached to a conical baffle. The mirrors and support structures are made of beryllium. Several variants on the Yardstick theme have been explored in simulation, using the same structure but different optics and controls.

The Yardstick optical design is an off-axis 3-mirror anastigmat, with a small powered tertiary mirror. The quartenary is a deformable mirror (DM); cryogenic DM technology is being developed that should permit excellent performance over a range of temperatures and actuator densities. ¹² The DM is followed by a fast-steering mirror (FSM) for

guiding. The NIR camera optics include a pyramid mirror, which feeds 4 separate channels of the NIR camera, and an Offner relay, which directs the light to the detector. Alternative optical designs have also been pursued which limit FSM steering-induced errors: pupil distortion and steering-induced field distortion can be significant with large FSM angles. Optical solutions using 4 mirrors and 2 steering mirrors have been identified. ¹³

The WCT optics provide a versatile experimental platform for WFC development. As shown in Fig. 3, there are 2 DMs, one for aberrating and the other for correcting the WF, for testing Fine Phasing control. A slide-in mirror replaces the aberrator DM with a 3-segment mirror, which is used to test Capture and Alignment and Coarse Phasing control modes. This feature is new and has not yet generated any data. The hardware is driven by GUI-based software, which permits remote operation over the internet, and can be modified to incorporate new algorithmic software. The WCT hardware will continue to evolve, incorporating more realistic hardware for experimentation and for use as a development platform for Nexus and NGST.

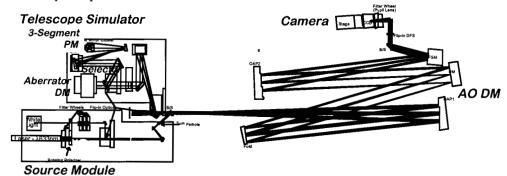


Figure 3. WCT layout

3.CAPTURE AND COARSE ALIGNMENT

Capture and Coarse Alignment begins at first light, following the initial deployment of the primary and secondary mirrors. The telescope is pointed at an isolated bright star, and the first pictures are taken by the Near IR camera. An example of what might be expected is shown in the upper left frame of Fig. 4, which shows the image of a single bright star taken with the primary mirror misaligned by random errors. The misalignments have standard deviations of 300 umin translation and 10 urad in tilt. As shown, only a few of the 9 segments reflect light onto the focal plane; the others are so misaligned as to send their spots off of the detector field of view. Those spots that do fall on the detector are blurred by defocus, showing fuzzy outlines of the the segment shapes.



Figure 4. Capture example. First image shows focal plane just prior to scanning Segment 2 into field; second image shows Segment 2 spot after detection; third image shows difference (WCT simulation).

It is the task of the Capture controller to identify which spots correspond to which segment, including those that fall off of the detector initially. It then aligns and focusses each segment individually to the Integrated Science Instrument Module (ISIM) and SM. The center segment is aligned first, and then used as a reference to which all other segments are aligned. Guiding begins once the center segment is captured and focussed.

The capture process begins by identifying segment spots that fall on the detector. A reference image is taken, and then a segment is moved a small amount, and a second frame is taken. Differences between the images identify the spot corresponding to that segment. The segment is then tilted to move its spot to the center of the field. If a segment is initially off the detector, the segment is scanned in a regular pattern in increments of angle slightly smaller than the

detector FOV. Eventually the segment spot is driven into the FOV and the segment is identified. Figure 4 shows a snapshot of a simulated WCT image sequence, where the second segment has just been driven onto the focal plane and identified.

After capturing a segment image, the segment is aligned and then focussed. The segment spot is first isolated, separating its spot from those of the other segments. The segment is then controlled in the piston DOF, maximizing the encircled energy within 3 successively smaller regions, converging when the maximum encircled energy within the smallest circle is found. The capture and alignment process is repeated until each segment spot is detected and focussed. Further examples are provided in Refs. 3 and 6.

4.REFERENCE SEGMENT ALIGNMENT

Following the capture, alignment and focussing of the center segment, and before focussing the other segments, alignment of the center segment to the SM and ISIM is accomplished. This is done with the outer segments masked or tilted out of the line of sight. It can be done using traditional focus/coma sweep techniques, or by using "prescription retrieval," or by using phase retrieval WF sensing as in the Fine Phasing control mode. Prescription retrieval is a parametric phase retrieval technique, where optical alignment and figure parameters are varied to match model-generated images to data. It is useful with high levels of aberration, and unlike the phase retrieval techniques discussed later, it can be used with broad-band illumination. It uses software called VSIM, which has been successfully applied to several different space instruments, including the Hubble Space Telescope and Mars Observer Camera. With appropriately diverse data VSIM is capable of separating the effects of misalignments from those of figure errors, and can distinguish between figure errors on multiple surfaces. Whichever technique is used, alignment of the center segment and SM to the ISIM should be achieved to within a few µm and µrad.

After Reference Segment Alignment the Capture and Alignment process is repeated for each of the outer segments, though using a different, slightly off-axis field of view for each, so as not to interfere with the light from the central segment. At the conclusion of this process, each segment is aligned to the reference segment to a small fraction of a pixel in angle and within the segment depth of focus in piston (about $15 \mu m$) – within the capture range of the Coarse Phasing controller described next.

Total dynamic range for the Capture controller is quite large, aided by the large detector array (4 amin on a side) planned for the Near IR camera. It is ultimately limited by the amount of time available for scanning, and possibly by confusion from multiple objects in a very large field. It should easily meet the NGST requirements 0f 5-10 mm in focus and a few mrad in angle.

5.COARSE PHASING

Now begins the coarse phasing process. First, the 8 outer segments are tilted out to point at specific spots well outside the center of the CCD. Then one outer segment is then tilted back in and coaligned with the center segment, so that their 2 spots overlie. The 2 segments are not in phase at this point, with perhaps 10 or more μ m difference between them. To detect this phase difference, a prism or grism is placed in the beam, creating a "dispersed-fringe sensor" (DFS) as illustrated on Fig. 5. The DFS disperses the light from the 2 coaligned segments up and down the detector, so that the light at any point on the detector is at a single wavelength. Phase differences between the 2 segments cause the overlapping images to produce interference fringes. The period of these fringes is a function of the absolute phase difference between the 2 segments. DFS techniques are used extensively in Michaelson stellar interferometry.

To illustrate the DFS, consider the field at the focus. Ignoring aberrations and diffraction and assuming equal segment illumination E_0 , the field at the each point x along the detector dispersion axis is

$$E = E_0 \exp\left(\frac{2\pi i L}{\lambda(x)}\right) \left(1 + \exp\left(\frac{2\pi i dL}{\lambda(x)}\right)\right) \tag{1}$$

The dispersing element is a grism placed in the filter wheel, with dispersion nearly linear with λ :

$$\lambda = \lambda_r x + \lambda_0 \tag{2}$$

The intensity pattern that results is

$$I = 2E_0^2 \left(1 + \cos\left(\frac{2\pi dL}{\lambda_x x + \lambda_0}\right) \right)$$
 (3)

The period can be measured as a function of x and matched to Eq. 3 to determine |dL|. Diffraction effects causes the real PSF for each wavelength to extend over a finite width -3 pixels in WCT. There is a constant phase shift between pixels, so the pattern of Eq. 3 is shifted between adjacent rows of pixels along the dispersion direction. The sign of this phase shift depends on the sign of dL; so the sign of dL is indicated by the angle of the null across the fringe. An example can be seen in Fig. 6, which shows a fringe from WCT phase-plate testing. This data is from a phase-plate with a 10 um segment step. The measured data matches the predicted fringe pattern very closely. The fringe analysis software tracks 3 rows of pixels along the fringe in order to determine the period and angle, thus measuring the piston and its sign in a single frame. 6

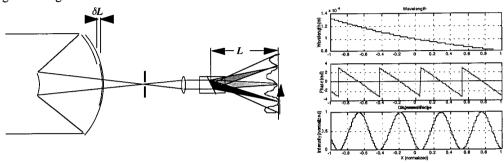


Figure 5. Dispersed-fringe sensor.

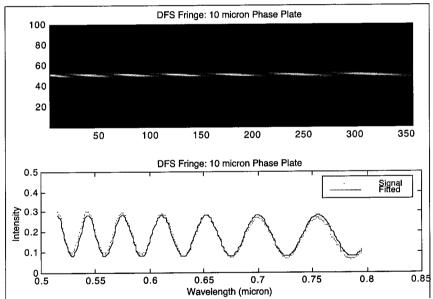


Figure 6. DFS test data, showing good agreement between prediction and data.

Visibility of the fringe can be reduced significantly for some orientations of the baseline between segments with respect to the grism dispersion axis. Especially for sparse apertures, sidelobe filling of the fringe nulls can occur if the dispersion axis approaches the baseline axis. Visibility is also better for one sign of dL, depending again on the angle between the dispersion and baseline, as sidelobe filling of the null will be greater for one sign than the other.

The DFS has a large dynamic range. The maximum detectable OPD difference is defined by the Nyquist sampling limit of the particular detector and the dispersion of the grism or prism. The grism dispersion is set to be sensitive to OPDs slightly larger than the focal depth of the segments. Larger OPDs are easily detected and corrected by the Capture and Alignment focus sweep.

Aberrations, including segment radius-of-curvature mismatches, tend to reduce the visibility of the interference fringes, but simulations indicate that this is not a significant problem for NGST specifications.⁶ Actuator errors define the accuracy with which the segments can be driven to their final positions.

The coarse phasing of segment pairs may conclude with a "white-light interferometry" (WLI) step. ^{3,6,14} Following the setting of the outer segment using the DFS, the DFS is removed from the beam by rotating the filter wheel, so that the detector once again sees a star image. The outer segment is then scanned in piston, and the peak intensity is recorded at each step. A correlation filter identifies the position with the highest peak intensity, and the segment is moved back to that point. WLI may not be required, as the dynamic range of Fine Phasing overlaps that of the DFS.

At this point, coarse phasing of the first outer segment to the central segment is complete. The coarse phasing process is then repeated for the next segment. The situation differs slightly for each successive segment, as the "reference segment" grows by the addition of successively more segments. Simulation indicates that this has the effect of increasing the "floor" of the DFS fringe pattern, while the absolute contrast increases slightly. When all segments have undergone coarse phasing, the PM is aligned and phased – to within a wave if the segment figure quality and the actuator accuracy are good.

6.FINE PHASING

Fine Phasing picks up where the Coarse Initialization leaves off: with the PM segments, SM and ISIM phased to within about a few waves. It ends with a diffraction limited telescope. All sensing is performed using the science cameras. Fine Phasing is split into 2 functions: WF sensing, which measures a high-resolution map of the wavefront; and WF control, which actuates the segment position and orientation and sets the deforming actuators on the DM and/or segments to minimize WF error.

Phase retrieval was chosen for WF sensing for several reasons:

- It has excellent performance, providing accurate, high spatial-resolution wavefront measurements. It has better performance bounds than Shack-Hartman sensors or curvature sensors. 16,17 WCT performance results shows repeatibility of better than $\lambda_{633}/100$ ($\lambda_{2000}/300$), far below actuator error levels.
- It has good dynamic range. The algorithm reported here has demonstrated 3+ waves range; when run with NGST's mid-IR camera at λ =15 μ m, this provides > 45 μ m peak-to-valley range, well within the sensitivity of Coarse Phasing. Other, parametric algorithms have even higher potential dynamic range. ¹⁰
- It works across segment discontinuities, modulo 2 pi, unlike approaches which measure derivatives of the WF (e.g., Shack-Hartman). By sensing at 2 or more wavelengths, it measures segment piston over a very large range.
- It uses the science cameras for sensing, rather than a WF sensor, has obvious cost, mass and complexity benefits.
- It does not require extraneous or non-common path optics, eliminating important sources of error and reducing calibration requirements.
- It allows separate, end-to-end calibration of each of the science cameras, at arbitrary field points.
- It is robust to noise and blurring effects.

The primary NGST WF sensing uses a "Modified Gerchberg-Saxton" (MGS) iterative transform phase retrieval algorithm. The classic Gerchberg-Saxton algorithm assumes an imaging system whose f number is known, with known detector pixel size and a known aperture mask, illuminated with monochromatic light at a known wavelength. It iterates to match a single in-focus image. It starts with a random guess at the phase in the exit pupil, which is combined with a pupil amplitude mask to form a complex-amplitude matrix representing an estimated field at the pupil. This is Fourier transformed forward to the image plane, generating an estimated image-plane complex amplitude matrix. The amplitude of the image-plane field is replaced by the square root of the image data, and then this new field is back-propagated to the pupil plane, where it is masked by the aperture function. The phase of this new field is the estimate of the WF phase. The new pupil field is transformed forward to the pupil, and the iteration continues. Convergence is indicated when the phase estimate does not change significantly from iteration to iteration. The GS algorithm is quite good at matching images; however, it is very sensitive to noise and is not guaranteed to find a unique solution.

The NGST MGS phase retrieval algorithm uses the Gerchberg-Saxton iteration as its inner loop, but with several modifications, as illustrated on Fig. 7. These include:Pupil image data is used to constrain the pupil field estimate. Pupil images are taken using a small flip-in lens located just in front of the science detector. By substituting the square root of the pupil image data for the estimated pupil amplitude, many unknowns are removed from the problem, with no loss in accuracy.

- Defocussed rather than in-focus images are used. An in-focus PSF puts almost all of its signal into a few tightly clustered pixels, underresolved in our case, where the signal is quickly eroded by digitization and blurring effects such as jitter. Defocussing spreads the image over many pixels, creating extended, lower contrast signatures for all aberrations. These wisps, tendrils, lumps and blobs, signalling hills and valleys in the optics, are large compared to the fixed size of the typical blurring kernel, hence are less degraded by blurring effects.
- Defocussing also reduces the contrast between low spatial-frequency information, contained in the bright core of
 the in-focus PSF, and high spatial-frequency information, normally in the dim sidebands of the in-focus PSF. In
 the defocussed PSF low and high frequency structures are spread across the image, with more equal illumination.
- Multiple images with known phase shifts are matched simultaneously. Using multiple images provides additional data without introducing new unknowns, provided that the diversity phase is accurately known. The MGS control software embeds the S-MACOS computer code operating on a detailed "as-built" prescription of the optical system to predict diversity phase as a function of whatever perturbation is introduced (Ref. 10). Diversity phase can be effected by defocusing, changing wavelength, or other means. Image iterations are run in parallel.
- À priori knowledge of the phase is subtracted from the iteration, which reduces the dynamic range of the iterate.
- Limits are placed on the iteration-to-iteration change of the estimate, damping the iteration.
- Phase unwrapping is used to improve the dynamic range of the phase retrieval beyond 1 wave. Many cases of interest will have WF errors that exceed 1 wave peak-to-valley at the phase retrieval wavelength, causing them to wrap, by taking their value modulo 2π . The MGS algorithm unwraps each separate image iterate separately, and then combines all iterates in a voting scheme, to help identify unwrapping artifacts. The MGS unwrapping algorithm is described in the next section.
- Estimates derived from data at multiple colors are processed together to resolve segment piston.

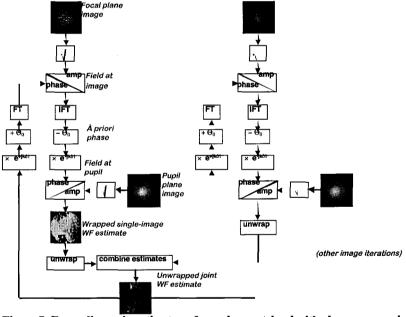


Figure 7. Focus-diverse iterative-transform phase retrieval with phase unwrapping.

The MGS inner loop starts with a random pupil phase estimate as before, but the amplitude is now combined with the square root of the pupil image to form the pupil field. The pupil phase then is shifted by 2 factors: the "known" à priori phase θ_0 and the "diversity phase" θ_{div} . The pupil field is propagated to the image plane with a Fourier transform; the amplitude of the image plane field is replaced by the square root of the image data; and then the field is inverse Fourier transformed back to the pupil. The à priori and diversity phase factors are then removed, and the the process is repeated. After about 10 inner-loop iterations, the pupil estimate stabilizes.

The MGS outer loop then takes the several image-specific pupil estimates and combines them in a weighted averaging scheme to develop a joint estimate of the pupil (Fig. 7). This is sent back to each of the inner-loop image

iterations, and these are repeated. After some number of outer loop iterations, the pupil phases are explicitly unwrapped prior to combining, so as to resolve 2π ambiguities in the estimate. The unwrapping code uses a simple, fast algorithm of limited accuracy – as opposed to the alternative, a complex, slow algorithm of limited accuracy! The algorithm compares steps between adjacent pixels in 3 wrapped angle estimates that are shifted in phase by $2\pi/3$, identifying wrap points by inconsistencies between the estimates. The unwrapped estimates are compared to identify unwrapping artifacts, which are resolved by voting. Overall, about 30 outer iterations are typically done.

Other algorithms can also be used. *Prescription retrieval*, ¹⁰ which drives a parametric model of the optical train to match out-of-focus images, provides a particularly useful complement to the MGS approach. Where MGS is monochromatic and requires phase unwrapping, prescription retrieval can work broad-band and can match highly aberrated data without phase unwrapping. For WCT, model parameters include DM actuators, so the DM correction is determined directly from the match; a WF estimate can be computed from the converged model and then used for the à priori phase factor in MGS. *Phase diversity* algorithms offers the ability to retrieve using images of extended objects. ¹⁵

A typical example of wavefront sensing using the WCT is shown on Fig. 8. Here the Simulator DM was deliberately aberrated, using random actuator commands. The images were taken using a 3 nm bandpass filter at 632.8 nm wavelength. Integration time was varied to nearly saturate the CCD at the brightest pixels. The images were processed using the MGS algorithm embedded in the WCT Executive Software, requiring about 5 minutes on a 4-processor workstation. The WF estimate shows a peak-to-valley error of 1.6 waves, with an RMS of 0.27 waves.

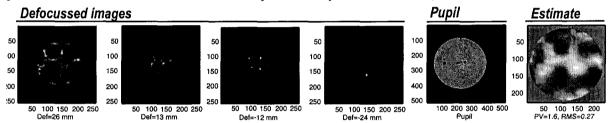


Figure 8. Images, pupil image, and resulting WF estimate for a typical WCT experiment.

Another example showing high dynamic-range records a series of actuator "pokes," as shown in Fig. 9. Here a pattern of 4 actuators on the AO DM is pushed up, starting with a low value (lower right plot) and proceeding in steps to a high value, corresponding to 5.2 waves peak-to-valley and 0.4 waves RMS WF error.

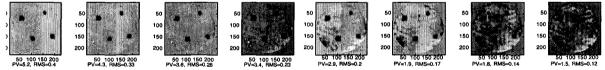


Figure 9. WF estimates obtained for a sequence of actuator "poke" patterns.

A third example, showing the excellent repeatibility of the WF sensing technique, is shown in Fig. 10. Here the WCT WF was flattened and left untouched for a few hours. The WF was measured 10 times during that period as shown. The mean of the 10 estimates was subtracted from each frame, with the results shown in the right side on Fig. 11. The estimates agree with a repeatibility of $\lambda/110$. The pixel-by-pixel standard deviation of the 10 frames is $\lambda/240$.

In testing, phase retrieval WF sensing has proven to be robust and reliable, even in conditions of relatively large turbulence and jitter errors. Figure 12 illustrates this by showing the WF sensing error vs. jitter for a Monte Carlo analysis of a 7-hex segmented configuration of the WCT. Each point on this plot represents 100 trials with different noise and aberrations, through the entire image generation and processing sequence. Above 0.2 pixels jitter, the WFS error drops smoothly, reaching $\lambda/50$ at 1 pixel jitter and $\lambda/30$ at 2 pixels. These results compare with WCT performance as indicated. Note that 4 images are better than 2, though this may be more because larger defocus values are used. The flattening of the curve at 0.2 pixels is likely due to the undersampling of the PSF in WCT. Simulations with critically-sampled PSFs show significantly better WFS performance.

Other examples and experiments are reported in Refs. 4-7. Overall accuracy using WCT data is about $\lambda/100$. Dynamic range is a few waves peak-to-valley – heroic measures can extend this. For NGST, which is equipped with NIR and MIR cameras, WF sensing can be done at wavelengths from under 1 μ m to over 15 μ m. Aberrations of a few

waves at a sensing wavelength of up to 15 μ m should be measureable, providing an overall dynamic range of about 50 μ m peak-to-valley. This provides considerable overlap with the Coarse Phasing accuracy of about 1 μ m. Ultimate accuracy at 1 μ m wavelength should be better than 10 nm.

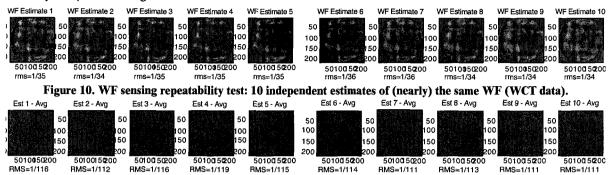


Figure 11. Deviation of each WF estimate from mean (WCT data).

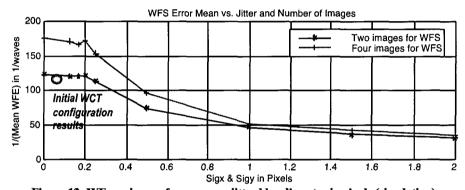


Figure 12. WF sensing performance vs. jitter blur diameter in pixels (simulation).

The wavefront control phase of fine figure initialization takes the estimated wavefront and uses it to determine new actuator commands for the segments, the SM and for the DM. The wavefront estimate is vectorized by stacking columns of the estimate matrix on top of each other, producing the wavefront vector \mathbf{w} . The wavefront \mathbf{w} is – for small motions – a linear function of the optical states \mathbf{x} , which includes rotation and translation degrees of freedom for each optic, plus deformation parameters. It is also a function of the control vector \mathbf{u} , which includes some of the rotation and translation degrees of freedom, plus the DM actuators. The linearized model of \mathbf{w} takes the form:

$$w = \frac{dw}{dx}x + \frac{dw}{du}u\tag{4}$$

Here the sensitivity matrices dw/dx and dw/du can be determined from computer models or by direct measurement – by poking the actuators and recording their influence on the WF, as in the example of Fig. 9.

An unconstrained control that seeks to minimize wavefront error squared is:

$$u = -G\overline{w} = -\left[\left(\frac{dw}{du}\right)^T \frac{dw}{du}\right]^{-1} \left(\frac{dw}{du}\right)^T \overline{w}$$
 (5)

This simple linear control law is noniterative and exact, subject to assumptions of linearity, and ignoring noise. Nonlinearities and constraints, such as relative and absolute actuator stroke limits, can be explicitly encompassed using different control formulations, most of which require iterative solution.²⁰ Noise performance of this control law is discussed elsewhere.³

A 36-segment telescope example is provided by the WCT Executive Software running in simulation mode (Fig. 13). The experiment begins by deforming and misaligning the segments, so the initial WF error is 7.5 μ m RMS, with a completely broken-up in-focus image, as illustrated in the left column of the figure. The image plots here are taken at 2 μ m wavelegth, sampled at f/28 with 27 μ m pixels. The initial Strehl ration (SR) is 0.2%. The control is computed in 2 parts, with the segments moved first, and the DM following up. The effect of the segment control is shown in the

middle column – the WF error is reduced somewhat, but more significantly, the segment edges are matched to create a smooth WF that is more effectively corrected by the continuous facesheet DM. Strehl following segment-only control in this example is 10%. Finally, the DM is used to peak the Strehl to 95% (rightmost column).

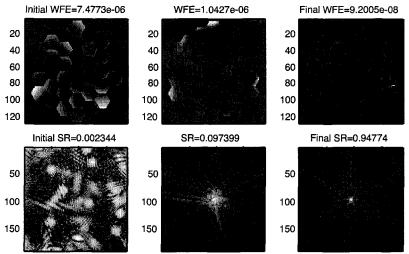
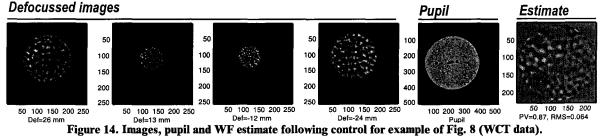


Figure 13. WFC example for a 36-segment NGST (simulation).

A second WF control example (Fig. 14) shows the result of controlling the example of Fig. 8. The WCT AO DM was used to compensate the random aberrations induced by the random actuation of the Simulator DM. The images show much smoother structure, and the post-control estimate is much improved (λ 15 vs. λ 4 RMS initially). Further iteration of the control process would improve this further. Overall WCT WF control performance has been good, λ 20 to λ 30 at λ =632.8 nm. The amount of residual WF error is a function of the initial error at low spatial frequency (fitting error) and the high spatial-frequency, sttic errors in the WCT optics and DM.



7.POST-CONTROL IN-FOCUS POINT SPREAD FUNCTIONS

The proof of WFC performance is the quality of the in-focus PSF after the WFC is completed. Typical WCT post-WFC PSFs are shown after flattening to about $\lambda/20$ at 632.8 nm in Figs. 15 and 16. Certain PSF characteristics are important to note. The first is a tight core with a high Strehl ratio. The second is a "dark hole" – a roughly square region with low scattered light immediately surrounding the core, extending out to a spatial frequency of roughly 1 over twice the actuator spacing – Nyquist for the DM. The dark region is itself surrounded by a "halo" of scattered light that cannot be removed by the DM, since it is due to aberrations with spatial frequency beyond the DM frequency cut-off, mostly DM fixed-pattern error. The PSFs are shown on a log10 stretch.

Model results agree well with the data. The model incorporates the retrieved WF, the measured pupil intensity, a slightly resolved source, and measured jitter and lab seeing effects. The latter effects were incorporated using a convolution model with a gaussian half-width of 0.5 pixel. The effect of the residual WF error is seen by comparison with the lower curve in the bottom left plot, which was computed with a perfectly flat WF. The major difference is that there is no halo in the latter case.

To better resolve the PSF, an image magnifier was set up in the lab. This uses an additional lens to blow up the PSF by 4.5 times. The result is seen in Fig. 16, which now clearly shows 8 Airy rings from the core to the edge of the dark

hole, where they are swamped by the halo of scattered light. Jitter and seeing effects were partially removed from this image using shift and add techniques, combining 68 short-exposure frames (integration time = 0.1 sec).

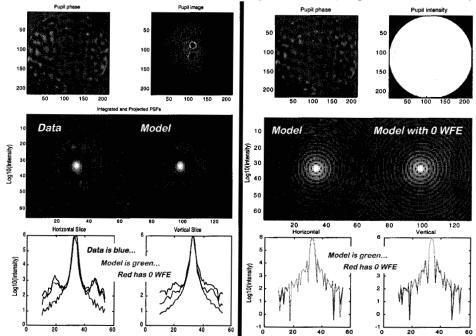


Figure 15. In-focus PSFs at 633 nm (left) and 2 um (right) (WCT data and simulations).

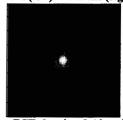


Figure 16. Magnified in-focus PSF showing 8 Airy rings to DM halo (WCT data).

A second example uses a simulated model of NGST as equipped with highly-actuated, deformable PM segments as designed by the U. of Arizona. A total of about 2800 actuators are used to compensate initial alignment and figure errors generated according to typical U. of A. measured large-mirror post-fabrication PSDs. The resulting PSF shows a deep, extended black hole, suitable (when used with a coronagraph) for finding planets around nearby stars. 21

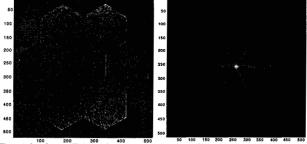


Figure 17. Corrected WF and in-focus PSF, for 7-segment U. of Arizona deformable PM (NGST simulation).

CONCLUSION

The wavefront control system described here is simple, robust, and accurate. By utilizing the science instruments for sensing it avoids expensive and complex dedicated sensors, while allowing for true end-to-end control and calibration in any of the science cameras. Performance is excellent, as demonstrated in the lab and in computer simulation.

ACKNOWLEDGEMENTS

The authors thank J. Britt, J. Deering, M. Fitzmaurice, J. Hagopian, C. Leboeuf, D. Robinson, and L. Wheeler of GSFC and R. Hein, R. Capps, D. Coulter, J. Trauger, D. Moody and K. Liu of JPL. This work was performed at the Jet Propulsion Laboratory, California Institute of Technology, under contract with the National Aeronautics and Space Administration.

8.REFERENCES

- 1. B. D. Seery, "Next generation space telescope (NGST)," Paper 3356-01, Kona HI (1998).
- 2. J. C. Mather, "NGST Science and Engineering Requirements," SPIE Paper 4013-87, Munich (2000).
- 3. D. Redding, S. Basinger, A. Lowman, F. Shi, P. Bely, R. Burg, G. Mosier, "Wavefront Control for the Next Generation Space Telescope," Paper 3356-??, Kona HI (1998).
- 4. D. Redding, S. Basinger, A. Lowman, F. Shi, C. Bowers, L. Burns, P. Davila, B. Dean, M. Fitzmaurice, J. Hagopian, C. Leboeuf, G. Mosier, T. Norton, B. Perkins, P. Petrone, L. Wheeler, M. Wilson, "Performance of the NGST Wavefront Control System," NGST Science and Technology Exposition, Hyannis MA (1999).
- 5. S. Basinger, D. Redding, A. Lowman, K. Liu, J. Lou, L. Burns, "Performance of Wavefront Sensing and Control Algorithms on a Segmented Telescope Testbed," SPIE Paper 4013-52, Munich (2000).
- 6. F. Shi, D. Redding, S. Basinger, A. Lowman, C. Bowers, M. Wilson, "DCATT Coarse Phasing Using Dispersed Fringe Sensing and White Light Interferometry," SPIE Paper 4013-53, Munich (2000).
- 7. C. Bowers, P. Davila, B. Dean, B. Perkins, M. Wilson, D. Redding, S. Basinger, A. Lowman, F. Shi, L. Burns, M. Fitzmaurice, T. Norton, P. Petrone, "Initial Test Results from the NGST Wavefront Sensing and Control Testbed," SPIE Paper 4013-116, Munich (2000).
- 8. A. Lowman, F. Shi, D. Redding, S. Basinger, C. Bowers, P. Davila, "Telescope Simulator for the DCATT Testbed," SPIE Paper 4013-56, Munich (2000).
- 9. C. LeBoeuf, P. S. Davila, D. C. Redding, D. R. Coulter, L. Pacini, "Deployed cryogenic active telescope testbed (DCATT): a wavefront sensing and control testbed for the next generation space telescope (NGST), Paper 3356-72, Kona HI (1998).
- 10. S. Sirlin and D. Redding, "VSIM," NASA Tech Briefs (1997).
- 11. G. E. Mosier, M. Femiano, K. Ha, P. Y. Bely, R. Burg, D. C. Redding, A. Kissil, J. Rakoczy, L. Craig, "Integrated modeling environment for systems-level performance analysis of the next generation space telescope," Paper 3356-08, Kona HI (1998).
- 12. M. Ealey, "Cryogenic Deformable Mirror Technology," NGST Science and Technology Exposition, Hyannis MA (1999).
- 13. S. Macenka, private communication.
- 14. S. Sirlin and D. Redding, "Modeling and Initialization of a Segmented Telescope," *Controls for Optical Systems*, SPIE 1696, pp. 243-252 (1992).
- 15. R.G. Paxman, T.J. Schulz and J.R. Fienup, "Joint Estimation of Object and Aberrations Using Phase Diversity," J. Opt. Soc. Am. A 9, 1072-85 (1992).
- 16. J. Cederquist, C. Wackerman, "Phase-retrieval error: a lower bound," JOSA, (4) 9, 1987.
- 17. J. Cederquist, J. Fienup, C. Wackerman, J. Robinson, S. Kryskowski, "Wavefront estimation from Fourier intensity measurements," JOSA, (6) 7, 1989.
- 18. MACOS Manual, JPL Document, 1999.
- 19. J. Burge, "Active Mirror Technology for Large Space Telescopes," SPIE Paper 4013-39, Munich (2000).
- 20. A.E. Bryson and Y.C. Ho, Applied Optimal Control, Halsted Press, 1969.
- 21. J. Trauger, M. Ealey, R.Bagwell, D. Moody, Y. Gursel, B. Gordon, "High-Order Wavefront Correction for High-Contrast Imaging," SPIE Paper 4013-49, Munich (2000).





Wavefront Control for a Segmented Deployable Space Telescope

David Redding, Scott Basinger, David Cohen, Andrew Lowman, Fang Shi

Jet Propulsion Laboratory, California Institute of Technology

Pierre Bely

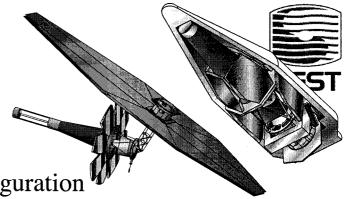
Space Telescope Science Institute

Chuck Bowers, Richard Burg, Laura Burns, Pamela Davila, Bruce Dean, Gary Mosier, Todd Norton, Pete Petrone, Brendon Perkins, Mark Wilson Goddard Space Flight Center, National Aeronautics and Space Administration

March 29, 2000

LSS

NGST Yardstick



- Nine rigid segments in a "flower" configuration
- Segments cryo-figured to under 1 wave ($\lambda = 2$ mm) at operating temperature
- Segments and SM deployed to 5 mm piston, 5 mrad tilt accuracy
- Segments actuated in rigid-body DOFs
- Deformable quartenary mirror provides means of correcting segment figure errors
- NIR and MIR cameras provide 1-16 mm imaging, can be used for WF sensing
- Very low temperature change across operating envelope
- Very low effective system CTE (may include active thermal control)
- Very low vibration and slew environment

A NASA Origins Mission

NGST Baseline WFC

NGST

- WFC functions are performed using the science cameras
- Control is split into distinct phases:
 - Initial Capture, Coarse Align and Coarse Phasing control follows deployment
 - WFE goes from mm to um
 - Fine Phasing follows initial phasing
 - WFE goes from um to nm
 - Fine Phasing is repeated throughout the mission
 - Dedicated observations or simultaneous with science observations, using other camera
- Figure is held passively during observation period

Timeline:	Deployment		
The plant of the p	Segment capture and coarse alignment		
Coarse Alignment And Phasing	Reference segment fine alignment		
	Segment 2 phasing: Dispersed-Fringe Sensing		
	Segment 2 phasing: White Light Interferometry		
	Segment 9 phasing: Dispersed-Fringe Sensing		
	Segment 9 phasing: White Light Interferometry		
Fine Phasing	Wavefront sensing and control		
Stability	Observations		
	0 First light Time	>	

Next Gener

A NASA Origins Mission

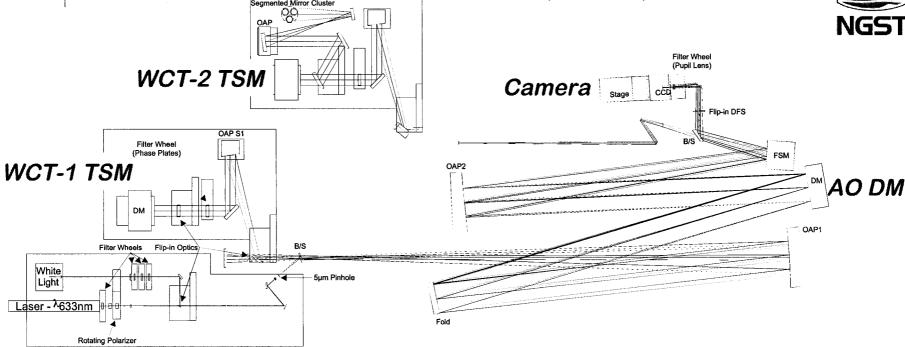
Validation Approach



- Extensive simulation at the full system level
- Demonstration in the lab using small optics
 - Validate control performance
 - Validate the simulations which predict control performance
- Validation in flight environment with Nexus
 - Validate stability
 - Validate operability

Wavefront Control Testbed (WCT)





WCT is used to develop WFC system, demonstrate performance

- Typical experiment uses Telescope Simulator (TSM) to inject errors
 - WCT-1: 97-actuator DM
 - WCT-2: 3 small segments
- Errors are sensed using WFS CCD camera
- Corrections implemented using AO DM and segments

Modeling and Simulation



- NGST models integrate optics, thermal, structures, controls
 - MACOS optics embedded in Matlab
 - IMOS structures, thermal, controls are Matlab toolboxes
- WFC algorithms embed models
 - Diversity phase, other phase retrieval factors computed from as-built optical prescription for selected field, filter, etc.
- WCT uses Model Server with physics and functional interfaces identical to actual hardware
 - Allows complete engineering of SW before HW is ready
 - Simplifies model validation
 - Same commands are used for model and hardware

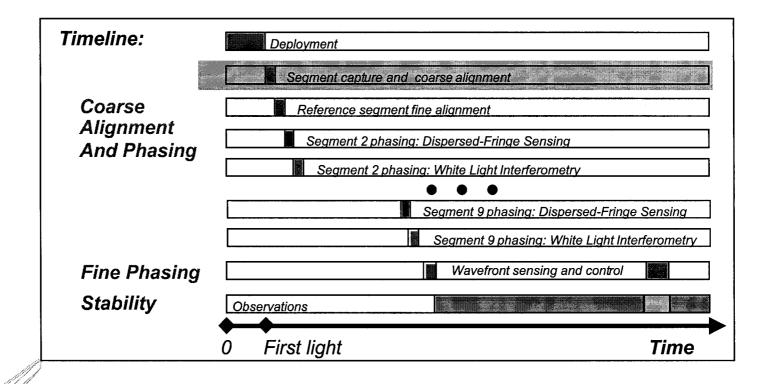


Origins Mission

Next Generation Space Telescope

Capture and Coarse Alignment



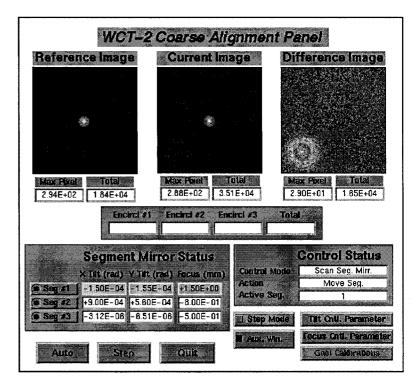


Capture and Coarse Alignment



- Performed at first light, while pointed at a bright, isolated star
- Segment is tilted slightly, frames differenced, and difference frame is thresholded
- If difference exceeds threshold, spot is centroided, and the spot is driven to the center of the field
- Otherwise, scan segment to next (4 amin) FOV and repeat

Focus each segment by maximizing 3-tier encircled energy metric



Notes:

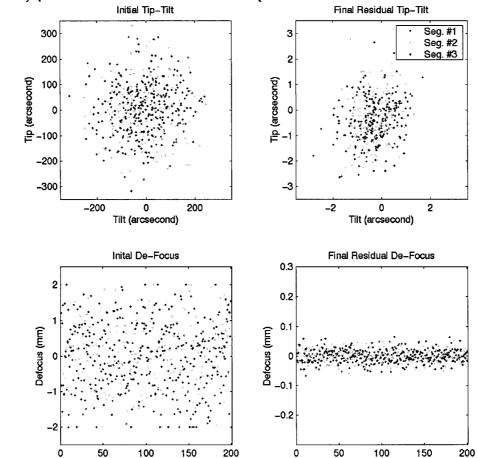
- Fine guiding not required
- Process can be run in parallel for multiple segments
- Coarse-stage actuation is adequate



Coarse Alignment Results (WCT-2 Model)

File Number





Segment errors reduced from millimeters to microns, well within capture range of Coarse Phasing

File Number

 Ultimate capture range limited by time, possibly by star-field confusion

9 0

u

S

atio

(C)

U

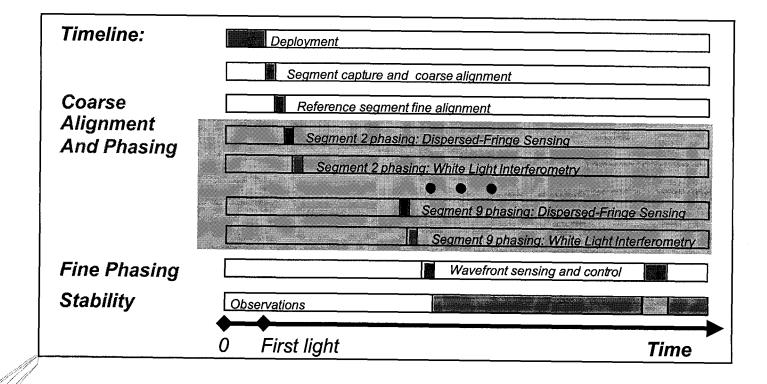
×

Next Generation Space Telescope

LSS

Coarse Phasing





Coarse Phasing: DFS Fringe Signals λ Increases Dark Band $\boldsymbol{\mathcal{X}}$ Spacing of fringes

50

40

60

0 p 0 U U) 0 **—**

> U ø

O

0.11

enerati

1200

800

600

400

10

20

30

DFS Fringe

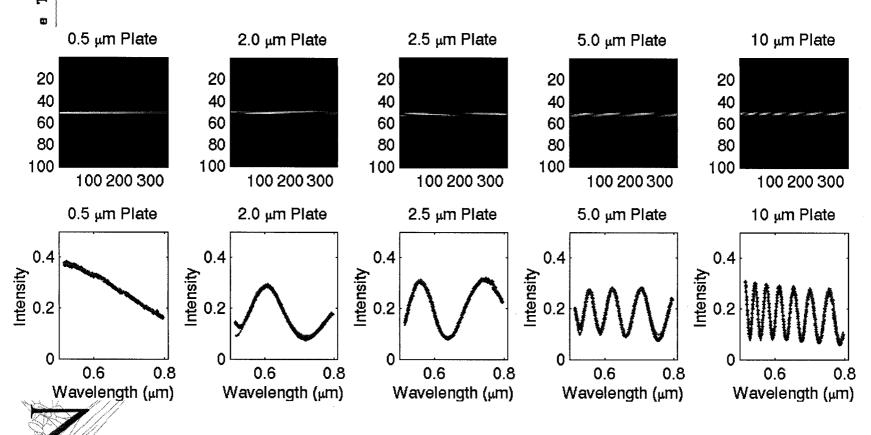
- indicates piston magnitude
- Angle of fringes indicates piston sign
- DFS Modeled Fringe: DCATT Model
- Wavelength range: $\lambda = 624.8 658.8 \text{ nm}$
- Piston error: $\delta L = 7 \mu m$

Telescope

A NASA Origins Mission

DFS Phase Plate Experiment Fringe Signals and Detection Fits







DFS Phase Plate Experiment Summary

Phase-plate piston (um)	DFS-measured piston (um)	DFS measurement error (um rms)
0.525	0.034	0.082
2.08	1.98	0.061
2.54	2.47	0.147
5.14	5.26	0.185
10.0	10.17	0.094

- DFS results agree with direct measurements by a white light interference microscope to better than $\lambda/3$
- DFS data and models agree
- Experiment provided successful test of WCT control software

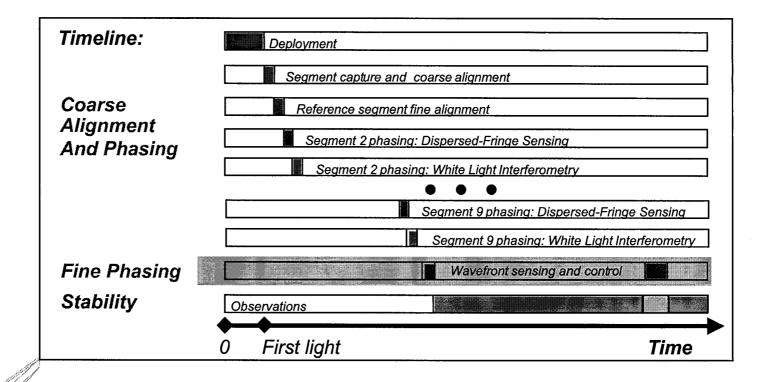
Others have also performed experiments demonstrating good DFS performance

Next Generation Space Telescope

A NASA Origins Mission

Fine Phasing







Á NASA Origins Mission

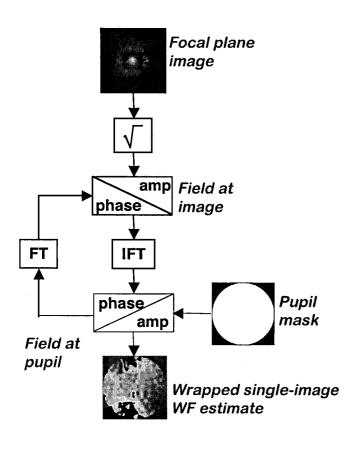
Why Phase Retrieval for WF Sensing?



- Phase-diverse phase retrieval (PR) chosen for WF sensing, because:
 - Excellent accuracy and high spatial resolution
 - Works across segment discontinuities, modulo 2 pi
 - Sensing at 2 or more wavelengths can resolve segment piston over a very large range
 - Robust to noise and blurring effects
 - Reasonable dynamic range when used with phase unwrapping
 - Large dynamic range when both NIR and MIR cameras used
 - Does not require a dedicated sensor
 - Can measure the entire optical train in all science cameras
 - Does not require extraneous or non-common path optics
 - No better performer

Gerchberg-Saxton Iterative-Transform PR





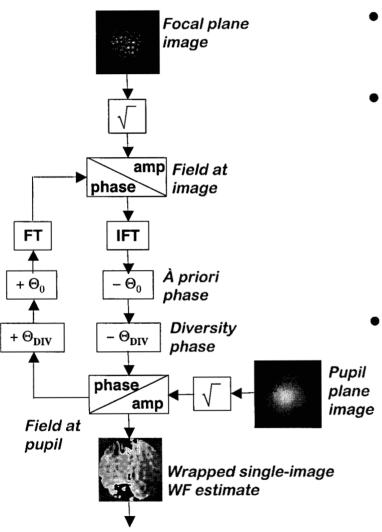
- Imaging system f/no., pixel size, aperture mask, λ all known
- Starts with a random guess at the phase in the exit pupil
- Iterates on pupil complex field until changes between iterates are small
- Pupil phase is angle of pupil field
- Produces high-resolution pupil map which matches image

But...

- Solution non-unique
- In-focus image susceptible to noise

Modified Gerchberg-Saxton Inner Loop

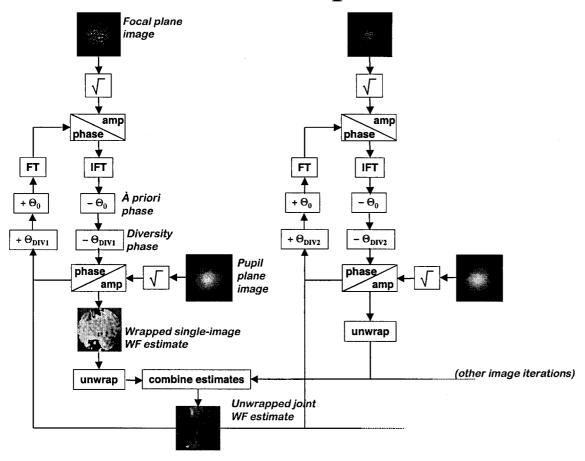




- Pupil image data replaces mask, halves number of unknowns
- Defocussed images improve visibility of aberrations
 - Spread out effects over many pixels
 - Reduce impact of jitter, other blurring
 - Reduce contrast between low, high-f effects
 - Subtracting known phase (Θ_0, Θ_{DIV}) from the phase iteration *reduces the iteration dynamic range*
 - Θ_0 is systematic across all images
 - Θ_{DIV} is difference between images from embedded MACOS model

MGS Outer Loop (cont.)

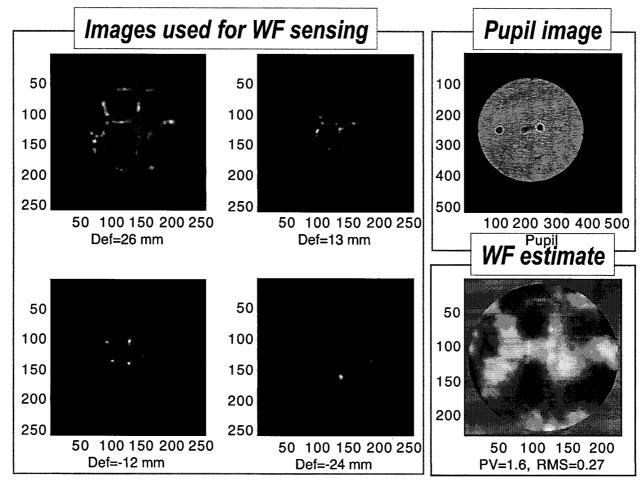




- Multiple images overdetermine solution to ensure uniqueness
 - Provides more data without introducing new unknowns
- Phase unwrapping allows estimation of WFE > λ
 - Joint unwrapping improves unwrapping robustness

Sensing a Random WF Error...





- Random aberration applied using telescope simulator DM
 - WFE = 1.6 waves peak-to-valley, 0.27 waves RMS

A NASA Origins Mission

H

S

eneratio

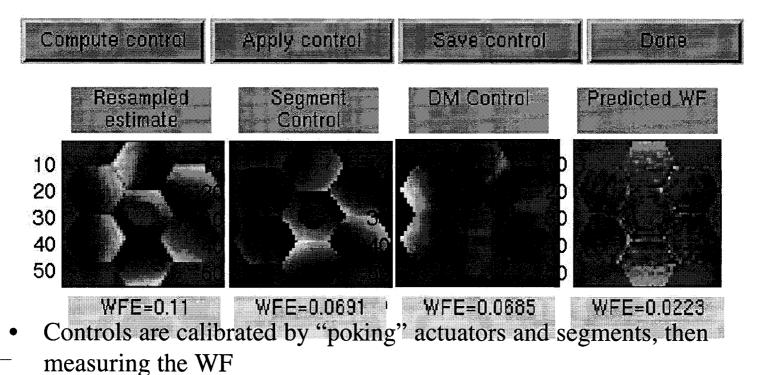
Ü

ext

ext Generation Space Telescope

WF Control





- WF_{poke} - WF = the effect of that actuator

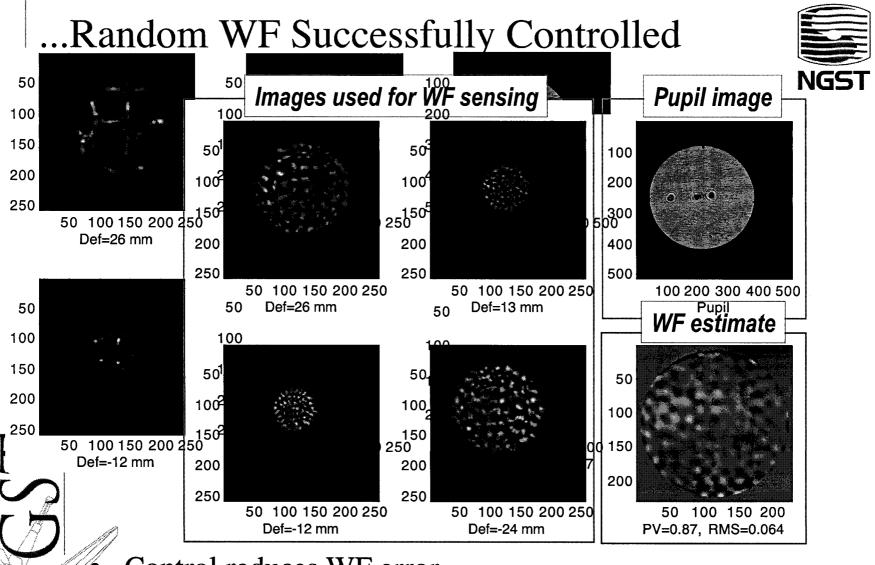
- Build up a sensitivity matrix recording the effect of all actuators on the WF

Control is determined by "inverting" the sensitivity matrix

Yields a gain matrix that transforms a WF into equivalent actuator commands

Control then applies the negative of these commands to null the WF

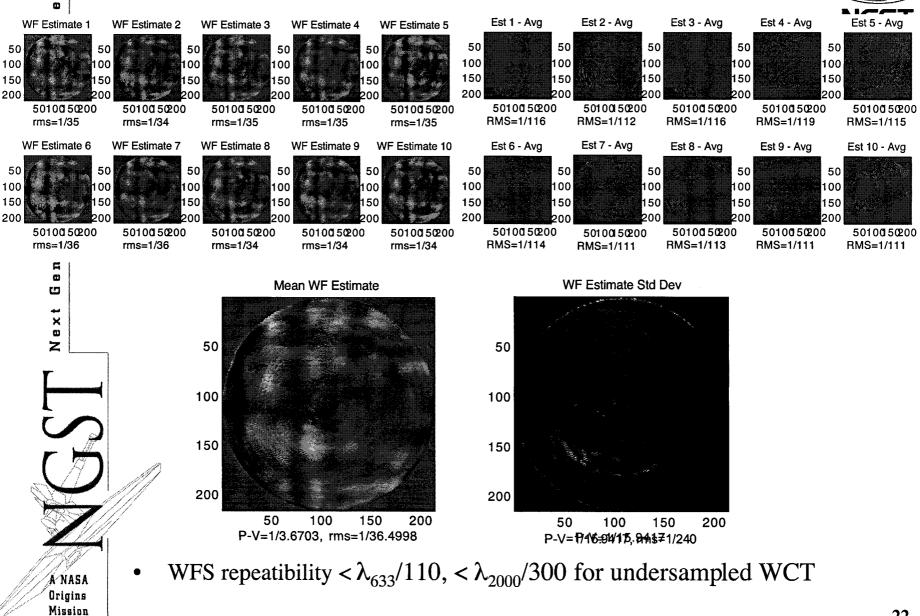
Constraints are imposed to protect the mirrors



Control reduces WF error

- Initial WFE = 1.6 waves peak-to-valley, 0.27 waves RMS
- After control WFE = 0.87 waves PV, 0.064 waves RMS

WFS Highly Repeatible



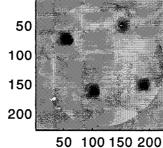
DM Pokes Show Good Dynamic Range



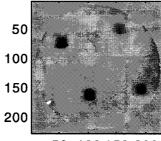
ext Generation Space Telescope

50 100 150 200 50 100 150 200

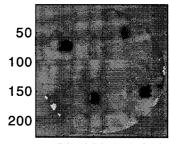
50 100 150 200 PV=5.2, RMS=0.4



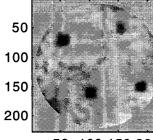
50 100 150 200 PV=4.3, RMS=0.33



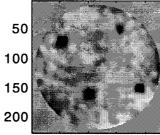
50 100 150 200 PV=3.6, RMS=0.28



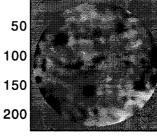
50 100 150 200 PV=3.4, RMS=0.23



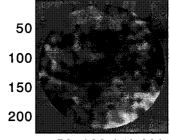
50 100 150 200 PV=2.9, RMS=0.2



50 100 150 200 PV=1.9, RMS=0.17



50 100 150 200 PV=1.8, RMS=0.14

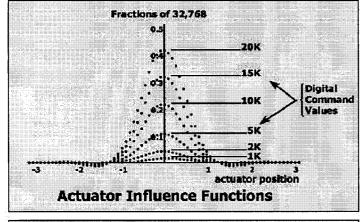


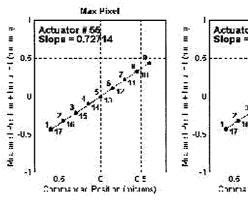
50 100 150 200 PV=1.5, RMS=0.12

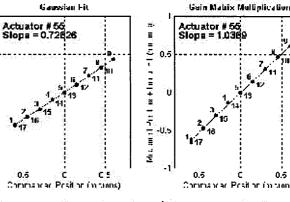
- DM actuator "poke" patterns provide a high spatialfrequency, high dynamic range test
- Pokes exceed 5 waves WF in this example

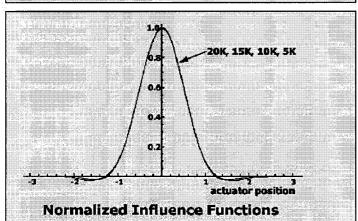
DM Calibration Summary

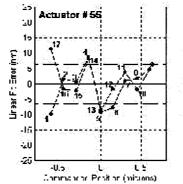


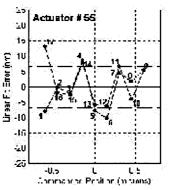


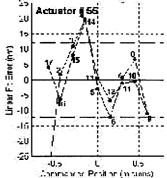












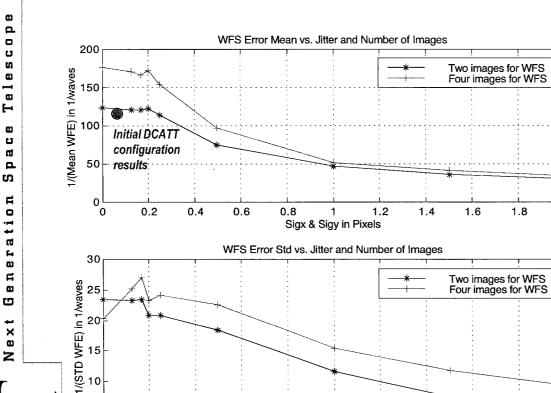


Results to date:

- Influence functions are linearly scalable
- Hysteresis and nonlinearity are minor effects
 - 0.5% in linear range about half-voltage position
- Repeatability of commanded positions averaged 2 nm (single test)

WFS Insensitive to Jitter





Monte Carlo simulation, 100 trials/pt

DCATT optics
Double-pass telescope
Random misalignment
WFE< 1 wave for each case
15 DN read noise
12 bits dynamic range

Phase retrieval parameters λ = 632.8 nm 2x oversampled Two images: Defocus = ±15 mm Four images: Defocus = ±15, ±7.5 mm 2 images run to full well

Modeling results indicate good performance possible even with significant jitter

1.6

1.8

1.4

• Born out by results using current WCT configuration

Sigx & Sigy in Pixels

Data at 0.1 pixel jitter

0.6

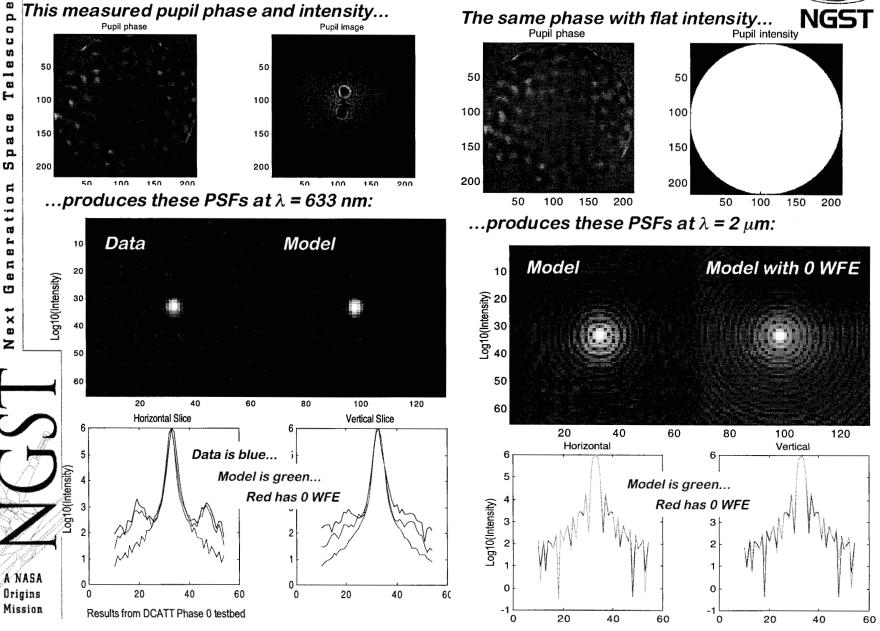
0.8

0.2

Reliable WFS in high jitter cases (0.4 pixel)

Deep In-Focus PSF at Vis and NIR

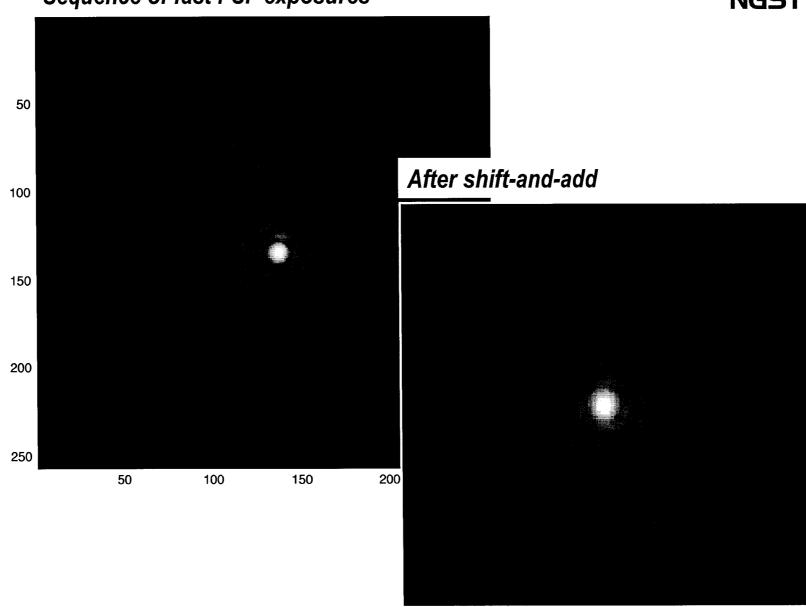




Magnified PSF

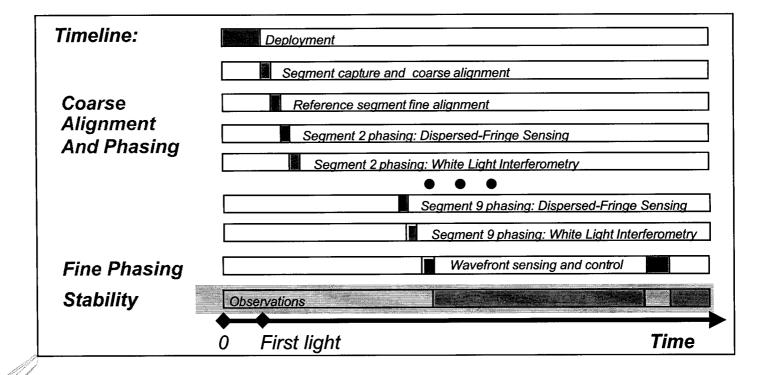
Sequence of fast PSF exposures





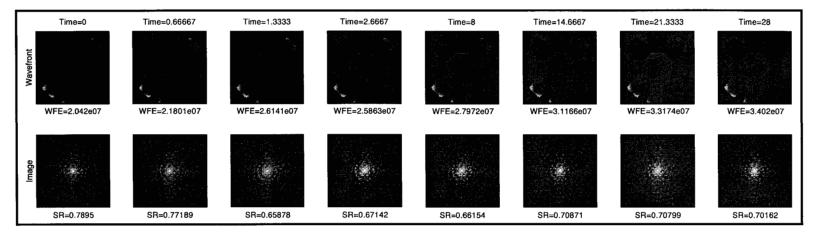
Stability



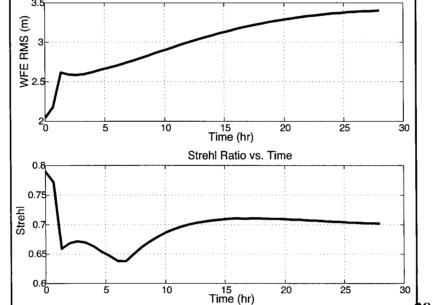


Thermal WF Stability: No Thermal Control





- WF control performed at hottest attitude
 - SR = 79%
- 1 hr slew to coldest attitude
- Steady state reached 28 hours later
 - SR = 70%



Wavefront Error vs. Time



ល

p

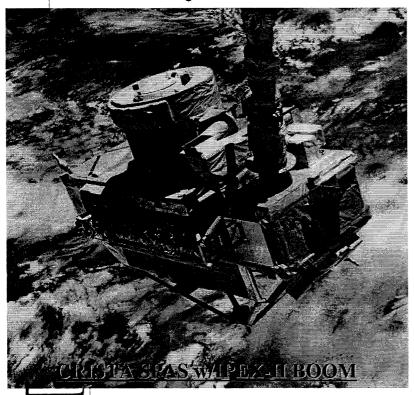
Ensuring Thermal Stability



- Better thermal and structural design will improve passive stability
- Active thermal control provides insurance
 - Further reduce thermal deformations
 - Keep a uniformly loaded structure to minimize microdynamics
- Two active thermal control strategies are being investigated:
 - 1. Use heaters to keep important temperatures *constant* at the normal onorbit "hot" condition
 - 2. Estimate WF error from measured temperatures, then control heaters to minimize WF error, subject to power limits
- Thermal models are updated using ground and space test data to ensure accuracy
- Repeating worst-case Yardstick attitude maneuver example:
 - Both controls kept WFE below 28 nm
 - Control 2 used 3% of the power required by control 1 (7 vs 210 mW)

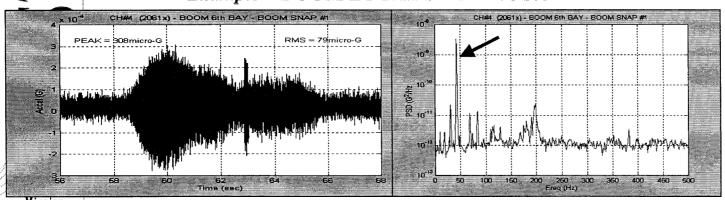
Microdynamics





- Microdynamics are sub-micron displacement, broad-band dynamical disturbances
- Caused by nternal strain energy release
- Relieves both transient and quasi-static loads (e.g., thermal strains, mechanism motion ...)
- Occurs in materials, latches, joints and other interfaces
- Exhibited as "SNAPS", high frequency localized disturbances
- Difficult to control actively

Example - BOOM LOCAL SNAP - 58 sec



Ensuring Microdynamical Stability



- To control microdynamics, NGST will...
 - Minimize through mechanical design
 - Minimize through stabilized thermal and mechanical environment
 - Prevent load relief by keeping load constant
- Microdynamics are hard to observe on the ground
 - Impeded by gravity effects
 - "Joint dominated" deployable structures can be more stable in space than on ground: IPEX showed 4% damping on-orbit, vs. <1% on ground
 - Masked by noisy lab environment
- NEXUS precursor mission will validate approach

A NASA

Mission

Conclusion



- Our validation plan is well underway, with key elements proven in hardware
- Control system development continues
 - Improve WFS dynamic range
 - Improve WFC constraint handling, optimize to encircled energy
 - Improve coarse alignment and phasing efficiency
- Focus on Nexus precursor mission